

# The van der Waals Epitaxy of High-Quality N-Polar Gallium Nitride for High-Response Ultraviolet Photodetectors with Polarization Electric Field Modulation

Yang Chen, Zhiming Shi, Shanli Zhang, Jianwei Ben, Ke Jiang, Hang Zang, Yuping Jia, Wei Lü, Dabing Li, and Xiaojuan Sun\*

High-quality and polarity-controlled III-nitride is crucial for realizing high-performance and new types of device designs with rich functionalities, but there are still many difficulties for obtaining N-polar III-nitrides till now. In this work, the van der Waals epitaxy of high-quality N-polar gallium nitride (GaN) is reported by innovatively inserting a thin MoS<sub>2</sub> layer. Due to the remission of thermal and lattice mismatch by the weak van der Waals force in 2D MoS<sub>2</sub> insert layer, the N-polar GaN exhibits high crystalline quality and reduced residual stress. The proposed atom deposition kinetics for the van der Waals epitaxy of the polarity-controlled aluminium nitride nucleation layer and GaN epilayer on the MoS<sub>2</sub> lighten the great potentiality for the application of similar 2D materials. The ultraviolet photodetector based on N-polar GaN possesses over seven times' response higher than that of the Ga-polar one, which is both beneficial from the high crystalline quality and efficient polarization electric field control of the N-polar GaN. Present work provides a new strategy for the polarity control of high-quality III-nitrides by the van der Waals epitaxy with a novel 2D insert layer, which would be also extended in other optoelectronic and electronic devices.

is restricted by the intrinsically large lattice and thermal mismatch between the epilayer and foreign substrate, which induces a mass of dislocations and the strong residual stress.<sup>[8]</sup> Generally, the large stress in III-nitrides triggers the risk for epilayer crack and the high-density dislocations act as carrier recombination centers and leakage channels, which would both lower the device performance and degrade its uniformity for the mass production. Traditional buffer layers including low-temperature aluminium nitride (AlN) nucleation layer,<sup>[9]</sup> periodic superlattice structure,<sup>[10,11]</sup> and Al metal film<sup>[12]</sup> have been widely applied, however, the total residual stress in epitaxial systems remain unchanged. In other words, the mismatch-induced dislocation and stress are partially confined in the buffer layer, and thus the optimization of crystalline quality and residual stress for III-nitride epilayers is limited. Recently,

## 1. Introduction


In the past few decades, gallium nitride (GaN)-based III-nitrides have exhibited great advantages in power electronic and optoelectronic devices, including quick chargers,<sup>[1,2]</sup> communication technologies,<sup>[3]</sup> light-emitting diodes,<sup>[4,5]</sup> and photodetectors.<sup>[6,7]</sup> However, the crystalline quality of heteroepitaxial III-nitrides

the high-quality and stress-free III-nitrides epitaxy on 2D layers (including h-BN and graphene) are developed, which is so-called as van der Waals epitaxy.<sup>[13–15]</sup> This innovation relies on the excellent stability and weak van der Waals interlayer interaction of 2D insert layers, which fundamentally solves the trouble induced by the heteroepitaxy. As the trade-off, the atomic flatness surface and scarce dangling bonds of h-BN and graphene have made difficulties in III-nitride nucleation. Unless the insert 2D layers are broken or atom-doped by specific treatments, including plasma or in situ nitridation, the epitaxial III-nitride could be in a high crystalline quality with the coalescent surface.<sup>[16,17]</sup>

Apart from the crystalline optimization of III-nitrides, it is known that the typical III-nitride with wurtzite crystalline structure has an inversion symmetry along the c-axis orientation, possessing two opposite polar faces of Ga-polar ([0001] direction) and N-polar ([000 $\bar{1}$ ] direction).<sup>[18]</sup> The spontaneous polarization vector of III-nitride is determined by the polarity orientation, and thus different types of charges would be generated. As a consequence, the optical as well as electrical properties of III-nitride can be adjusted by controlling the polarization orientation. Several works prove that the proper assembly of metal-polar and N-polar III-nitrides could invert

Y. Chen, Z. Shi, S. Zhang, J. Ben, K. Jiang, H. Zang, Y. Jia, W. Lü, D. Li, X. Sun  
 State Key Laboratory of Luminescence and Applications  
 Changchun Institute of Optics  
 Fine Mechanics and Physics  
 Chinese Academy of Sciences  
 Changchun 130033, P. R. China  
 E-mail: sunxj@ciomp.ac.cn

W. Lü  
 Key Laboratory of Advanced Structural Materials  
 Changchun University of Technology  
 Changchun 130012, P. R. China

 The ORCID identification number(s) for the author(s) of this article can be found under <https://doi.org/10.1002/aelm.202100759>.

DOI: 10.1002/aelm.202100759

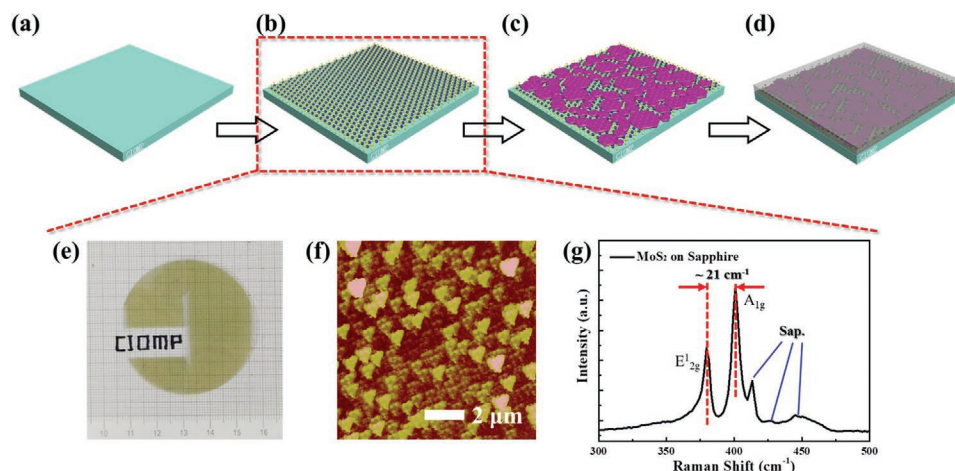


**Figure 1.** a–d) Schematic diagram of the van der Waals epitaxy for AlN nucleation layer and GaN epilayer on the 2D MoS<sub>2</sub> insert layer. e) Photograph of the MoS<sub>2</sub> layer on a 2 in. sapphire wafer. f) AFM and g) Raman measurement of the as-grown MoS<sub>2</sub> layer.

the internal electric field and adjust the position of 2D electron gas, aiming at high performance Schottky barrier diodes,<sup>[19]</sup> second harmonic generators,<sup>[20,21]</sup> as well as ultraviolet lighting-emitting diodes.<sup>[22,23]</sup> Besides, the chemical stability and surface energy of Ga-polar and N-polar are also in significant difference, which are used in nanostructure fabrications and highly sensitive sensors.<sup>[24,25]</sup> Therefore, the polarity control of III-nitride is very meaningful for realizing high-performance and new types of device designs with rich functionalities.

Up to now, the metal-polar III-nitride is commonly used because of the higher crystalline quality and more mature growth technique compared to the N-polar one. Generally, the metal-polar III-nitride is grown on c-sapphire substrates by metal-organic chemical vapor deposition (MOCVD). To invert the polarity of III-nitrides, the careful nitridation of sapphire substrates and an additional low-temperature AlN nucleation layer are both essential.<sup>[26–28]</sup> However, the sapphire substrate with low misorientation angle provides limited migration ability during the growth of N-polar III-nitrides, inducing the low nucleation density and following un-coalescent surface. Hence, special sapphire substrates with misorientation angle larger than 2° are adopted for the epitaxy of N-polar III-nitrides with enhanced crystalline quality.<sup>[29,30]</sup> Otherwise, high concentration Mg atoms incorporated into III-nitrides could generate stacking faults, thus inducing the polarity inversion into the N-polar.<sup>[31,32]</sup> This attempt allows the integration of N-polar III-nitrides on the metal-polar with a vertical junction, but the existence of partially inverted domains and faceted interfaces in N-polar materials are unsatisfactory. Most recently, Liu et al. demonstrated the epitaxy of N-polar GaN epilayer on the graphene modified sapphire substrate.<sup>[33]</sup> The N atoms irradiation of graphene by the molecular beam epitaxy (MBE) first produces C–N bonds, leading to the preferred N-polar GaN growth. It should be noted that the crystalline quality of N-polar GaN epilayers needs to be improved, and the complicated nitridation treatment of graphene with MBE is inevitable by this strategy. In other words, the direct epitaxy of high-quality N-polar III-nitrides by the widely used MOCVD system is still challenging.

In present work, the direct epitaxy of high-quality N-polar GaN epilayer is achieved by the van der Waals epitaxy process with a MoS<sub>2</sub> insert layer, which is reported for the first time to our best knowledge. After the deposition of a low-temperature AlN nucleation layer, the Ga-polar GaN on bare sapphire substrates (S-GaN) and N-polar GaN with MoS<sub>2</sub> insert layer (M-GaN) are simultaneously grown under the same growth procedure in MOCVD system, making the easy modulation of GaN polarities and excellent compatibility with the present GaN epitaxy technique. The excellent crystalline quality of N-polar M-GaN with released residual stress is severally confirmed by the X-ray diffraction, Raman spectra, and photoluminescence (PL) spectra measurement. The surface potential and wet etching results have identified the uniform polarity inversion for the GaN epilayer with MoS<sub>2</sub> insert layer. The growth mechanism of the polarity inversion for N-polar M-GaN is demonstrated by the first-principles calculations, showing that the out-of-plane S atoms in MoS<sub>2</sub> possessed stronger interaction with Al species due to the big electronegativity difference, and the interlayer distance as well as binding energy ( $E_b$ ) for the N-polar AlN configuration on the MoS<sub>2</sub> insert layer is lower. Comparing to that of the Ga-polar S-GaN, ultraviolet photodetectors (UV PDs), by integrating the N-polar M-GaN with graphene, obtain the enhanced response of 86.3 A W<sup>−1</sup>, which is attributed to the high crystalline quality of GaN epilayer as well as the modulation of interfacial potential difference and direction in the device. This work shows a new strategy for the direct van der Waals epitaxy and polarity control of high quality N-polar III-nitrides, which would also generate abundant capabilities for various designed devices.

## 2. Results and Discussions

### 2.1. The van der Waals Epitaxy of High-Quality GaN Epilayers with Released Stress

**Figure 1a–d** shows the van der Waals epitaxy process for GaN with a MoS<sub>2</sub> insert layer. First, for the in situ growth of 2D

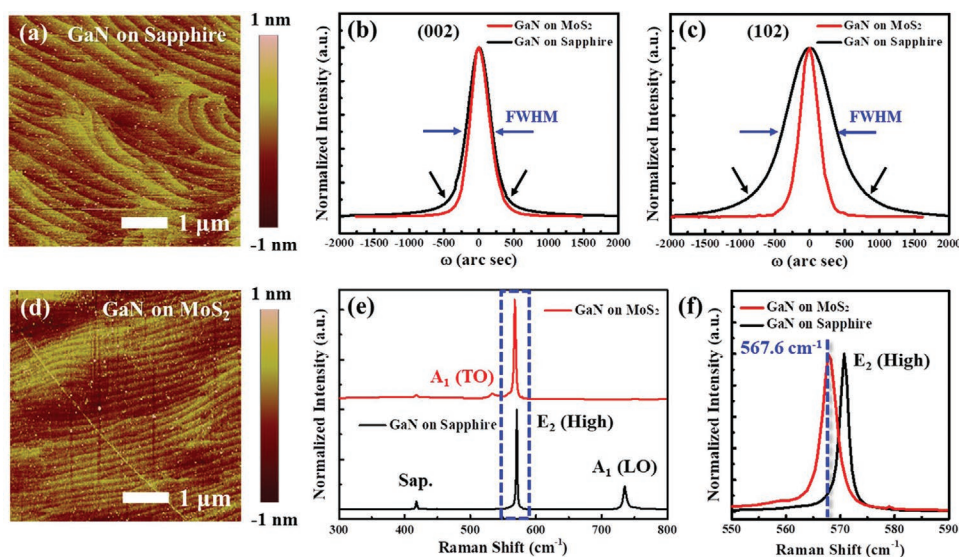


**Figure 2.** a) AFM images of the S-GaN and d) M-GaN. b) XRD rocking curves of the S-GaN and M-GaN with (002)  $\omega$ -scans and c) (102)  $\omega$ -scans. e) Raman spectra of S-GaN and M-GaN. f) The  $E_2$  (High) mode position of S-GaN and M-GaN compared to stress-free GaN.

MoS<sub>2</sub> insert layer, the pre-evaporated 2 nm MoO<sub>3</sub> film on a 2 in. sapphire substrate is reacted with the sulfur powder in a low-pressure chemical vapor deposition (LPCVD) system. The photograph of MoS<sub>2</sub> layer on a 2 in. sapphire wafer is shown in Figure 1e. Furthermore, the MoS<sub>2</sub> insert layer with triangle crystalline grains fully covers the sapphire substrate, and the crystal domain sizes are  $\approx 1 \mu\text{m}$  (Figure 1f). The properties of as-grown MoS<sub>2</sub> film are evaluated by Raman spectra (Figure 1g); the typical in-plane mode ( $E_{2g}^1$ ) and out-of-plane mode ( $A_{1g}^1$ ) of MoS<sub>2</sub> are located at 379.6 and 400.9 cm<sup>-1</sup>, and the sharp  $E_{2g}^1$  and  $A_{1g}^1$  bands with minor full width at half maximum (FWHM) of 5.2 and 4.9 cm<sup>-1</sup> demonstrate the high crystalline quality of MoS<sub>2</sub>.<sup>[34,35]</sup> Besides, the frequency difference of  $A_{1g}^1$ – $E_{2g}^1$  is  $\approx 21 \text{ cm}^{-1}$ , which implies that the MoS<sub>2</sub> possessed a bilayer nature.<sup>[36]</sup> The epitaxy of GaN is carried out on both sapphire substrates with and without the MoS<sub>2</sub> coverage by the MOCVD, in which the exactly same growth procedure is applied. As shown in Figure 1c,  $\approx 40 \text{ nm}$  low-temperature AlN nucleation layer is primarily deposited at 940 °C, aiming at the protection from MoS<sub>2</sub> thermal decomposition and reduction of dislocation density in the later GaN epitaxy. **Figure 2a,d** exhibits the original surface morphology of the S-GaN and M-GaN measured by atomic force microscope (AFM), respectively. Both of the samples have typical atomic step morphology with the root-mean-square roughness (Rq) of 0.358 nm (S-GaN) and 0.367 nm (M-GaN), in which the M-GaN with MoS<sub>2</sub> insert layer possesses the higher density of atomic steps with the shorter distance and orderly orientation.

The crystalline quality of S-GaN and M-GaN are evaluated by the rocking curves of X-ray diffraction (XRD), as shown

in Figure 2b,c. The XRD rocking curves FWHM for the (002)  $\omega$ -scan and (102)  $\omega$ -scan are positively correlated to the screw dislocation ( $N_{sc}$ ) and edge dislocation density ( $N_{ed}$ ) of epitaxial materials, respectively.<sup>[37,38]</sup> For the S-GaN, the FWHM of (002)  $\omega$ -scan and (102)  $\omega$ -scan are calculated to be 420 and 873 arc sec. As the comparison, the M-GaN exhibits the decreased FWHM of 342 and 328 arc sec. Therefore, the FWHM of the (102)  $\omega$ -scan for the M-GaN decreases over 500 arc sec with respect to the S-GaN, achieving the suppression of edge-related dislocation density in the M-GaN. The related dislocation density can be estimated from the following equation:<sup>[39]</sup>

$$N = \frac{\beta^2}{4.35 \times b^2} \quad (1)$$

where  $\beta$  is the FWHM of XRD rocking curves and  $b$  is the length of dislocation Burgers vector. In this way, the  $N_{sc}$  and  $N_{ed}$  of S-GaN are calculated to be  $3.55 \times 10^8$  and  $4.06 \times 10^9 \text{ cm}^{-2}$ , while the dislocation density decrease to  $2.35 \times 10^8$  and  $0.57 \times 10^9 \text{ cm}^{-2}$  for the M-GaN. The detailed parameters for the XRD measurement of GaN epilayers are summarized in **Table 1**. The suppression of dislocation formation is efficient by inserting the 2D MoS<sub>2</sub> film because of the weak van der Waals interaction between the MoS<sub>2</sub> layers, which induces the remission of intrinsic lattice mismatch between the sapphire substrate and GaN epilayer.

The S-GaN and M-GaN epilayers are further investigated by Raman spectra with a 532 nm laser source, as shown in Figure 2e,f. Since the energy of exciting photons is lower than the bandgap energy of GaN ( $\approx 3.4 \text{ eV}$ ), the measured Raman

**Table 1.** The XRD and Raman summaries of Ga-polar S-GaN and N-polar M-GaN.

Sample	FWHM (002) [arc sec]	FWHM (102) [arc sec]	$N_{sc}$ [ $10^8 \text{ cm}^{-2}$ ]	$N_{ed}$ [ $10^9 \text{ cm}^{-2}$ ]	$\Delta E_2$ [ $\text{cm}^{-1}$ ]	Residual stress [GPa]
Ga-polar S-GaN	420	873	3.55	4.06	3.1	1.21
N-polar M-GaN	342	328	2.35	0.57	0.2	0.08



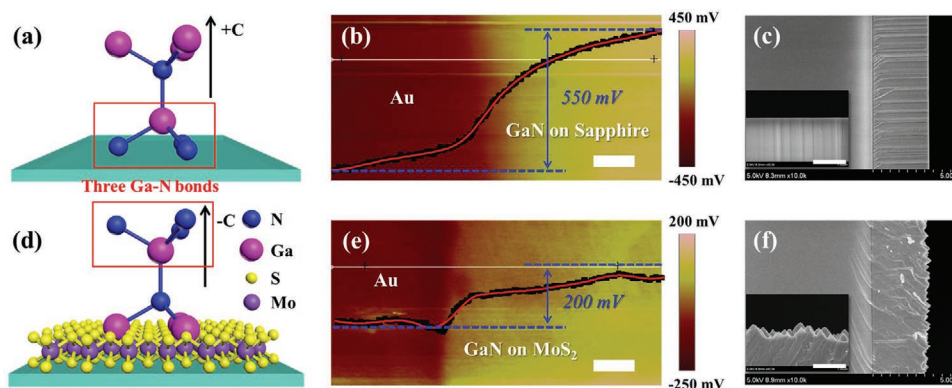


**Figure 3.** a) Schematic diagram of the Ga-polar GaN unit cell on sapphire substrates with [0001] direction and d) N-polar GaN unit on the MoS<sub>2</sub> insert layer with [0001] direction. b) Surface potential of the S-GaN and e) M-GaN measured by KPFM with Au as the basis reference. The scale bar is 10  $\mu\text{m}$ . c) SEM images of the S-GaN and f) M-GaN after the chemical etching by NaOH solution. Insets of (c,f) are the enlarged etching surface.

spectra works in the off-resonance condition. The hexagonal GaN with wurtzite structures belong to the part of  $C_{6v}$  symmetry group, and thus there are optical modes of  $A_1(z) + 2B_1 + E_1(x,y) + 2E_2$  at the  $\Gamma$  point of Brillouin zone.<sup>[40]</sup> Among these optical modes, the  $A_1$  and  $E_1$  modes are polar, which can split into the longitudinal optical (LO) mode of  $A_1(\text{LO})$ ,  $E_1(\text{LO})$ , and the transversal optical mode (TO) of  $A_1(\text{TO})$ ,  $E_1(\text{TO})$ . Otherwise, the  $B_1$  and  $E_2$  modes are non-polar, and the  $B_1$  mode is silent to the Raman scattering. Apart from the  $A_{1g}$  mode of sapphire at 418  $\text{cm}^{-1}$ , only the  $A_1$  and  $E_2$  modes appear for the GaN epilayer, and the absent of  $E_1$  modes is attributed to the selection rule for the geometry of Raman test. The  $A_1(\text{TO})$  mode of M-GaN is observed at 533.5  $\text{cm}^{-1}$ , however, the  $A_1(\text{LO})$  mode located at 735.4  $\text{cm}^{-1}$  acquired from the S-GaN is unavailable for the M-GaN. Previous works demonstrate that the high free carrier concentration in GaN crystal could form plasmon waves, which interacts with the LO phonons and further cripple this mode.<sup>[41]</sup> The higher carrier concentration is possible for the M-GaN assuming the lower incorporation energy for O atom impurities. This assumption would be subsequently cleared out by the photoluminescence (PL) and Hall measurements in the following parts.

The Raman  $E_2$  (High) mode is very sensitive to the biaxial strain, making it as an effective damage-free strategy to evaluate the residual stress in the GaN epilayer. Assuming that the  $E_2$  (High) mode of stress-free bulk GaN is located at 567.6  $\text{cm}^{-1}$ ,<sup>[38]</sup> the corresponding  $E_2$  (High) modes of S-GaN and M-GaN blue shift to 570.7 and 567.8  $\text{cm}^{-1}$  with the  $E_2$  (High) position difference ( $\Delta E_2$ ) of 3.1 and 0.2  $\text{cm}^{-1}$ , as shown in Figure 2f. The residual stress ( $\sigma$ ) in GaN epilayers can be estimated from the following equation:<sup>[42]</sup>

$$\Delta E_2 = K \times \sigma \quad (2)$$

where the stress coefficient of  $K$  is recognized as 2.56  $\text{cm}^{-1} \text{GPa}^{-1}$ . In this way, the S-GaN and M-GaN both suffer from the compressive stain by the underneath sapphire substrate, and the residual stress is calculated to be 1.21 and 0.08 GPa, respectively. Above results suggest that the efficient stress release is achieved for the M-GaN by inserting a 2D MoS<sub>2</sub> layer. It should be noted that the internal stress of

heteroepitaxial GaN can be relaxed by the formation of dislocations and stacking faults. Since the dislocation density is significantly reduced for the M-GaN, the efficient stress release could be attributed to the remission of thermal/ lattice mismatch between the GaN epilayer and sapphire substrate by the MoS<sub>2</sub> insert layer, which is consistent with the previous works about the van der Waals epitaxy of III-nitrides with graphene as the buffer layer.<sup>[12–15]</sup> Besides, the FWHM of M-GaN  $E_2$  (High) mode is broad compared to that of the S-GaN, proving the unintentional impurities incorporation and enhanced phonon-defect scattering, which is in accordance with the missing of  $A_1(\text{LO})$  mode in the M-GaN.

## 2.2. The Polarity Control of GaN Epilayers by the MoS<sub>2</sub> Insert Layer

The wurtzite GaN unit cells with Ga-polar and N-polar are shown in Figure 3a,d, which are identified as +c [0001] and -c [0001] along the growth direction. For the Ga-polar GaN, three Ga-N bonds of one Ga atom face toward the sapphire substrate, while the N-polar GaN by mirroring the unit cell of Ga-polar GaN makes the three Ga-N bonds of one Ga atom facing toward the free space. The surface potential of Ga-polar and N-polar GaN crystal is different because of the different polarization direction and background carrier concentration.<sup>[43,44]</sup> Herein, Kelvin probe force microscope (KPFM) is applied to evaluate the surface potential of S-GaN and M-GaN, as shown in Figure 3b,e. Thin Au films are both deposited on these two samples, severing as the basis potential reference. The uniform potential distributions are observed for the S-GaN and M-GaN, which imply the consistent polarity for the as-grown GaN epilayers. The surface potentials of S-GaN and M-GaN increase by  $\sim 550$  and 200 mV compared to that of referenced Au film, and thus the potential difference is calculated to be a large value of 350 mV between these two samples. The indeed higher surface potential of S-GaN compared to M-GaN reveals the polarity or carrier concentration difference.

As mentioned above, the chemical stability of Ga-polar and N-polar GaN is very different. Previous works report that only the N-polar GaN can be removed after the wet chemical etching

**Table 2.** The Hall measurement results of Ga-polar S-GaN and N-polar M-GaN at room temperature.

Sample	Carrier concentration [atoms cm <sup>-3</sup> ]	Mobility [cm <sup>2</sup> V <sup>-1</sup> s <sup>-1</sup> ]	Type	Sheet resistance [ $\Omega$ sq <sup>-1</sup> ]
Ga-polar S-GaN	$6.44 \times 10^{17}$	147	N	188
N-polar M-GaN	$5.98 \times 10^{18}$	84	N	27.7

process.<sup>[45]</sup> In this way, the S-GaN and M-GaN are both disposed with the NaOH solution at 85 °C for 60 min in order to identify the polarities of GaN epilayers. The thickness of the etched S-GaN and M-GaN is measured by the cross-sectional SEM to evaluate the etching effect (Figure 3c,f). The S-GaN maintains the original thickness of  $\approx 3.2$   $\mu\text{m}$  as well as the smooth top surface boundary, proving the nature of Ga-polar face. However, the top surface of the M-GaN changes from flatness into roughness with numerous nanostructured hillocks, which is consistent with the AFM measurements in Figure S1, Supporting Information. Meanwhile, the thickness of M-GaN decreases to  $\approx 3$   $\mu\text{m}$ . From the above results, it is specific that the M-GaN epitaxy on the MoS<sub>2</sub> insert layer is an N-polar GaN crystal. To further confirm the large-area polarity distribution uniformity of the Ga-polar S-GaN and N-polar M-GaN, the dynamic surface variation during NaOH etching is collected by OM at the same position (Figure S2, Supporting Information). As expected, the surface of S-GaN on bare sapphire substrate is consistent during the etching process, proving its uniform Ga-polar distribution (Figure S2a–c, Supporting Information). As the comparison, the surface of M-GaN appears with numerous etched pits, and its size and density are enlarged as the function of etching time (Figure S2d–f, Supporting Information). Under the same OM lighting intensity, the M-GaN images with enhanced darkness are observed. This is attributed to the optical scattering effect of the nanostructured hillocks induced by the chemical etching of N-polar M-GaN, and proving by the SEM images in Figure 3f.

The optical properties of S-GaN and M-GaN with the opposite polarities are measured by PL spectra with a 266 nm laser excited source at the room temperature, as shown in Figure S3, Supporting Information. The peak position of near-band-edge emission for Ga-polar S-GaN and N-polar M-GaN is located at 362 and 365 nm, respectively. According to the peak position of stress-free GaN at 365.8 nm,<sup>[46]</sup> the N-polar M-GaN is on the verge of unstressed condition, and the results agreed with the Raman measurement in Figure 2f. Here, the weak yellow peak appears at the wavelength of 550 nm for the N-polar M-GaN, and the corresponding intensity ratio of near-band-edge emission to yellow peak is  $\approx 13$ . The yellow peak originates from the point defect of Ga vacancy ( $V_{\text{Ga}}$ ) and O substituting on N site ( $O_{\text{N}}$ ) complexes ( $V_{\text{Ga}}-O_{\text{N}}$ ) in the M-GaN since the O atoms incorporation energy on the N-polar GaN is lower than that of the Ga-polar GaN, suggesting by the theoretical calculation.<sup>[47]</sup> Time-resolved PL (TRPL) decay spectra are employed to study the exciton recombination kinetics of Ga-polar S-GaN and N-polar M-GaN, as shown in Figure S4, Supporting Information. The decay lifetime for S-GaN and M-GaN are summarized in the inset of Figure S4, Supporting Information, and both of the two decay times are shorter for the M-GaN, which are 46 and 223 ps. These results demonstrate the fact that numerous O atom impurities incorporate into the N-polar

M-GaN and serve as the capture center for the photo-excited excitons, which further facilitate the recombination process. The reduction of carrier lifetime is also familiar for the Si-doped and Mg-doped GaN by increasing the doping concentration, as proved by the early works.<sup>[48,49]</sup> Up to now, the origins of O atom impurities are still unidentified, but several possible sources including precursors, sapphire substrates, and residual air in the reaction chamber might be responsible.

Hall measurement is carried out to investigate the electrical properties of unintentionally doped Ga-polar S-GaN and N-polar M-GaN at the room temperature, and the corresponding electrical parameters are summarized in Table 2. Both of the S-GaN and M-GaN have n-type conduction with electrons as the majority carrier. The carrier concentration of N-polar M-GaN reaches up to  $5.98 \times 10^{18}$  cm<sup>-3</sup>, possessing almost one order of magnitude higher than that of the Ga-polar S-GaN. Therefore, an extremely low sheet resistance of 27.7  $\Omega$  sq<sup>-1</sup> is achieved for the N-polar M-GaN. The O atom impurities incorporated into the GaN epilayers act as shallow donors, generating the majority of electron concentration as well as the PL yellow peak (Figure S3, Supporting Information). The point defects of  $O_{\text{N}}$  in the N-polar M-GaN might be evolved as follows: the abundant N dangling bonds at the outer face of N-polar M-GaN are first etched away by the hydrogen, and thus forming the N vacancy ( $V_{\text{N}}$ ). Then, the  $V_{\text{N}}$  offers the opportunity for capturing the O atom impurities.<sup>[28,45]</sup> Moreover, the Hall mobility of N-polar M-GaN with the higher carrier concentration decreases to 84 cm<sup>2</sup> V<sup>-1</sup> s<sup>-1</sup>. For the abundant O impurity shallow donors in N-polar M-GaN, the easy ionization would generate both free electrons as well as positively charged O ions. This provides an additional Coulomb potential field around the ionized O impurities, and thus destroying the periodic potential field of GaN lattices. In this way, the motion direction for free carriers could be changed by the Coulomb potential related to ionized O impurities, which is identified as the ionized impurity scattering. The scattering effect hinders the transportation of carrier in N-polar M-GaN, reflecting by the decreased carrier mobility.<sup>[28,50]</sup>

### 2.3. The Polarity Control Mechanism for the GaN Epilayers

The low magnification cross-sectional image of N-polar M-GaN epilayer with the thin AlN nucleation layer on the MoS<sub>2</sub> covered sapphire substrate is measured by transmission electron microscopy (TEM), as shown in Figure 4a. The sequence of layered structure is confirmed as the sapphire substrate, MoS<sub>2</sub> insert layer, AlN nucleation layer, and GaN epilayer from the bottom to top, which also exhibits clear boundaries between these adjacent layers. A high-resolution TEM (HR-TEM) cross-sectional image of layered sapphire/MoS<sub>2</sub>/AlN/GaN structure is also presented (Figure S5,

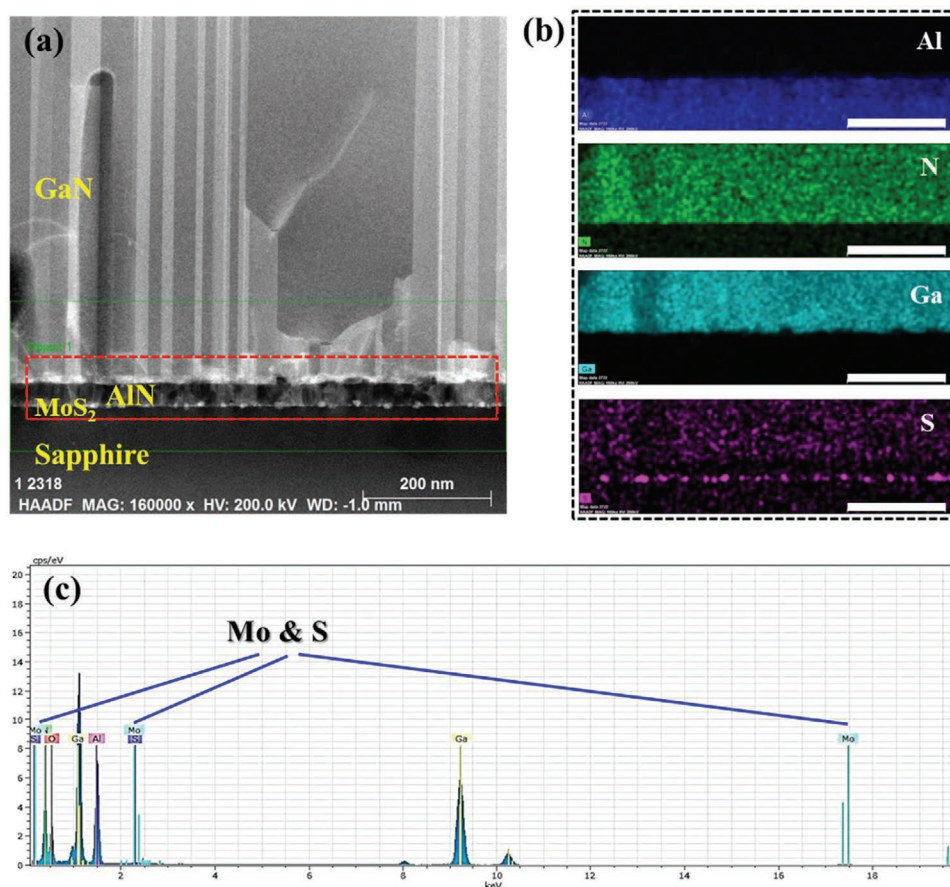


**Figure 4.** a) Low magnification cross-sectional TEM image of N-polar M-GaN and b) the corresponding EDS mapping of Al, N, Ga, and S elements extracted from the TEM image, as marked by the red dash line. c) Statistics of the elements at the interface of sapphire substrate and AlN nucleation layer by EDS. The scale bar in (b) is 200 nm.

Supporting Information). Based on the HR-TEM image, the thickness of AlN nucleation layer is  $\approx 40$  nm. Moreover, a continuous thin insert layer between the sapphire substrate and AlN nucleation layer is observed, as marked by the white arrow in Figure S5, Supporting Information. The thickness of the insert layer is  $\approx 1.5$  nm, which is consistent with the value of bilayer MoS<sub>2</sub> film. To identify the chemical components of this epitaxial structure, the energy dispersive spectroscopy (EDS) mapping images of Al, N, Ga, and S elements are established, as shown in Figure 4b. According to the distribution of Al, N, and Ga atoms, the interfaces of sapphire/AlN and AlN/GaN can be figured out, as marked by the red dash line in Figure 4a. The mapping of S atoms in MoS<sub>2</sub> proves that the MoS<sub>2</sub> insert layer is mainly located at the interface of sapphire substrate and AlN nucleation layer, while limited parts of them diffuse into the epilayers by the later high-temperature epitaxy process of M-GaN in the MOCVD system. The EDS measurement is further carried out at the local position of MoS<sub>2</sub> insert layer, focusing at the interface of sapphire substrate and AlN nucleation layer. As shown in Figure 4c, the element statistics reveal both strong Mo and S peaks, implying the existence of MoS<sub>2</sub>. It can be deduced that the pre-deposition of a thin layer AlN nucleation at low-temperature on the MoS<sub>2</sub> film suppresses its decomposition.

According to the present epitaxial structure, the polarity of AlN nucleation layer is crucial for inducing the polarity inversion of M-GaN because it is primarily grown on the MoS<sub>2</sub> insert layer. Here, the N-polar M-GaN with the AlN nucleation layer is chemically etched in the hot NaOH solution for a long enough time of 5 h, in which the reaction can penetrate from the top M-GaN layer into the AlN nucleation layer. The surface morphology of the sapphire/MoS<sub>2</sub>/AlN/GaN after the 5 h NaOH etching is measured by AFM (Figure S6a, Supporting Information). The typical area of etched sample has a clean and smooth surface, possessing a low Rq of 0.31 nm. From the comparison with the nanostructured hillocks of N-polar M-GaN after etching in NaOH solution for 60 min (Figure 3f), the AlN and GaN epilayers are fully etched away by the NaOH after 5 h. For large-area evaluation, the surface morphology of etched sapphire/MoS<sub>2</sub>/AlN/GaN is further measured by OM (Figure S6b, Supporting Information). Although few hexagonal hillocks remain (circled by the yellow dash line), nearly whole of the observed area is etched away, and thus exhibiting the uniformly bright field of view.

Raman spectra has identified the chemical component of the remained and etched areas (Figure S6b, Supporting Information), which are named as Remain and Clean-1 to Clean-5 in Figure S6c, Supporting Information. The typical E<sub>2</sub> (High)



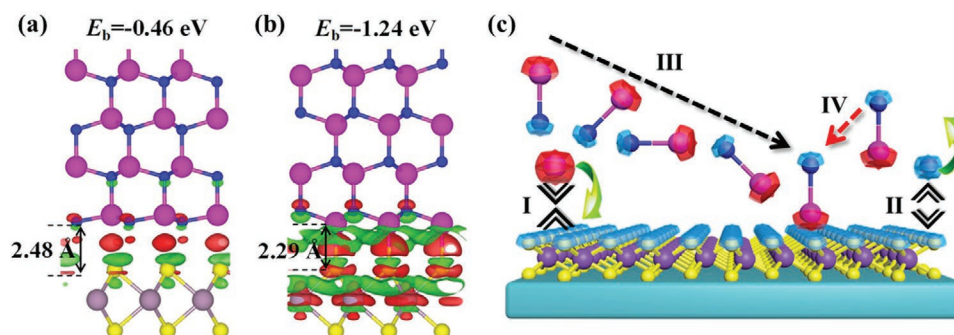


**Figure 5.** The interaction and binding energies of a) Al-polar or b) N-polar AlN nucleation layer on the MoS<sub>2</sub> insert layer. The interlayer distances and the contour of charge differences at interfaces are also plotted. The Al, N, Mo, and S atoms are represented by purple, blue, wine, and yellow balls. The isosurfaces are set to  $1.5 \times 10^{-3} \text{ e } \text{\AA}^{-3}$ ; the red and green are positive and negative values. c) Schematic diagram of the atom kinetics for the N-polar AlN epitaxy on the MoS<sub>2</sub> insert layer.

mode located at  $567.8 \text{ cm}^{-1}$  proves that the few hexagonal hill-ocks belong to the GaN material, which is attributed to the being of local unconverted Ga-polar GaN domains because of its insensitivity to the NaOH etching. For the clean areas, five randomly distributed points are selected for the accurate measurement. All these positions exhibit identical modes as the comparison with that of the bare sapphire substrate, implying that both the AlN nucleation layer and GaN epilayer are cleanly removed by NaOH after the 5 h etching. It should be mentioned that the typical modes of MoS<sub>2</sub> insert layer are also absent, and one can assume that the MoS<sub>2</sub> layer might separate from the sapphire substrate due to the weak van der Waals interaction after the harsh environment and longer enough processing time in the NaOH solution. According to the above results, it is clear that the N-polar epilayer begins inversion as the AlN nucleation layer first deposits on the MoS<sub>2</sub> insert layer. More importantly, nearly full polarity inversion for the III-nitride epilayers (both for the AlN and GaN) is achieved by simply inserting the 2D MoS<sub>2</sub> layer.

Based on the first-principles calculations, we calculate the  $E_b$  of N-polar and Al-polar AlN slabs on the MoS<sub>2</sub> insert layer to reveal the interaction between the AlN nucleation layer and underneath MoS<sub>2</sub> film, as shown in Figure 5a,b. The  $E_b$  are  $-1.24$  and  $-0.46 \text{ eV}$  per formula for the N-polar AlN (N-AlN) and Al-polar AlN (Al-AlN) on the MoS<sub>2</sub> insert layer, respectively. Here, the smaller  $E_b$  indicates the strong interaction of two contacted materials, and thus the N-AlN on the MoS<sub>2</sub> insert layer (N-AlN@MoS<sub>2</sub>) is more stable than that of the Al-AlN on the MoS<sub>2</sub> insert layer (Al-AlN@MoS<sub>2</sub>). This is attributed to the different charge transfer behavior at the interfaces because of the asymmetric structures for S and Mo atom layers of MoS<sub>2</sub>. For the N-AlN@MoS<sub>2</sub>, the interface composes by the Al atoms and S atoms; the strong charge transfer from the AlN nucleation layer to the MoS<sub>2</sub> insert layer can be observed because of their big electronegativity difference (Figure 5b). From the comparison, the charge transfer is weaker between the Al-AlN@MoS<sub>2</sub> interface than that at the N-AlN@MoS<sub>2</sub> interface, resulting in the weaker interaction between the Al-AlN nucleation layer and the MoS<sub>2</sub> insert layer. This trend is also reflected by the interlayer distances, showing that the N-AlN nucleation layer possesses the smaller interlayer distance ( $2.29 \text{ \AA}$ ) with the underneath MoS<sub>2</sub> insert layer ( $2.48 \text{ \AA}$  for the Al-AlN). Therefore, the theoretical

calculations demonstrate that the AlN nucleation layer prefers to be N-polar configuration on the MoS<sub>2</sub> insert layer.

As schematically shown in Figure 5c, the atom kinetics of the N-polar AlN epitaxy on the MoS<sub>2</sub> insert layer is proposed. Due to the valence electrons accumulation around the surface of S atoms in the Mo–S bonds of MoS<sub>2</sub> insert layer, the Coulomb interactions of the S atoms and Al atoms are stronger than that with the N atoms.<sup>[51]</sup> In this way, the Al atoms prefer to absorb on the MoS<sub>2</sub> insert layer (Process I) while the N atoms tend to desorb from its surface (Process II), showing the higher reaction activity between the Al and S atoms. During the chemical reaction in the MOCVD system, the species of Al–N pairs are formed. For the Al–N pairs with N atoms toward the underneath MoS<sub>2</sub> film, the rotation driven by the Coulomb interaction would appear (Process III), which finally results in the bonding of Al and S atoms. In addition, the Al–N pairs with Al atoms toward the MoS<sub>2</sub> film can be directly deposited (Process IV). According to the process of atom kinetics, a trend of Al atoms pre-deposition on the MoS<sub>2</sub> insert layer has induced the polarity inversion of AlN nucleation layer. As the result, the later epitaxy of GaN epilayer on the N-polar AlN nucleation layer is also in N polarity, which well matches with the experimental results of N-polar GaN epitaxy by inserting a MoS<sub>2</sub> layer in the MOCVD system. We consider that 2D materials composed of atoms with large electronegativity differences, such as WS<sub>2</sub>, gC<sub>3</sub>N, and gC<sub>3</sub>N<sub>4</sub>, might be also suitable for the epitaxy of N-polar nitrides.

#### 2.4. High-Response UV PDs Based on the High-Quality and Polarity-Controlled GaN Epilayers

The excellent worth of polarity modulation for van der Waals epitaxy high-quality GaN is verified by the UV PDs with enhanced performance. The schematic diagram of the cross-sectional device structures are exhibited in the insets of Figure 6a,d. The CVD-grown monolayer graphene is transferred onto the Ga-polar S–GaN and N-polar M–GaN as the carrier transport channel, which can facilitate the separation of photo-generated carriers in the GaN absorber and improve the carrier collection efficiency. The Raman spectra of graphene on the Ga-polar S–GaN and N-polar M–GaN are measured (Figure S7,

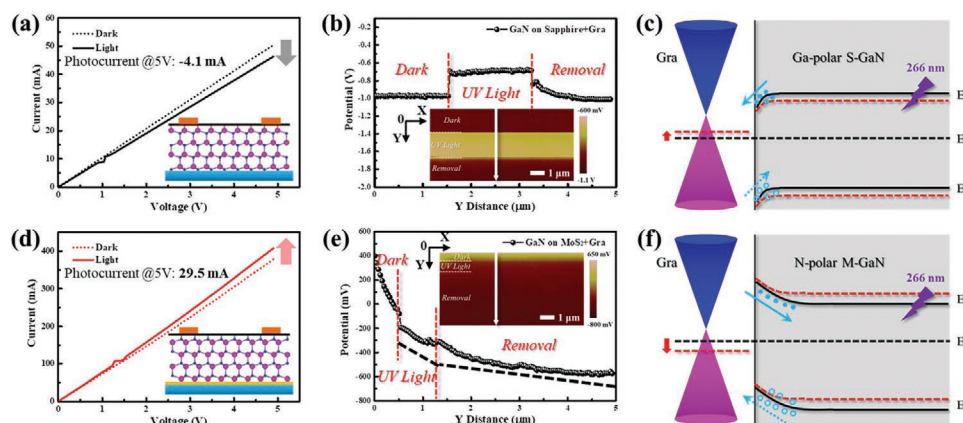


**Figure 6.** a) Current at the dark and light conditions as the function of scan voltage for the UV PDs based on Ga-polar S-GaN and d) N-polar M-GaN. Insets are the corresponding cross-sectional schematic diagram of UV PDs. b) Surface potential variation of the UV PDs based on Ga-polar S-GaN and e) N-polar M-GaN measured by the light-assist KPFM. c) The energy level distribution between graphene and Ga-polar S-GaN and f) graphene and N-polar M-GaN at the dark and light conditions.

Supporting Information), and both of the typical bands of graphene and GaN appear. The stronger intensity of 2D band compared to that of the G band proves the monolayer nature of transferred graphene.<sup>[52]</sup> Here, a pair of Au electrodes is deposited on graphene as the contact pads for device measurement, which also determines the UV PDs photosensitive area.

As shown in Figure 6a,d, the current of UV PDs are measured at dark and light (266 nm laser, power density of 3.8 mW mm<sup>-2</sup>) conditions with the scan voltage varied from 0 to 5 V, respectively. The dark current of the UV PDs based on the N-polar M-GaN reaches up to 378 mA, which is much higher than that of the Ga-polar S-GaN (50.4 mA). This comes from the higher background electron concentration and decreased sheet resistance of N-polar M-GaN, and it agrees with the results measured by Hall test (Table 2). The photocurrent of the UV PDs is defined as:

$$I_{ph} = I_{light} - I_{dark} \quad (3)$$

where  $I_{light}$  and  $I_{dark}$  are the current of UV PDs measured at the light and dark conditions. Hence, the photocurrent of UV PDs based on the Ga-polar S-GaN and N-polar M-GaN are calculated to be -4.1 and 29.5 mA. The response of UV PDs can be calculated from the following equation:

$$R = \frac{|I_{ph}|}{P \times A} \quad (4)$$

where  $P$  is the power density of irradiated UV light, and  $A$  is the photosensitive area of UV PDs. The corresponding response is calculated to be 12 and 86.3 A W<sup>-1</sup> for the UV PDs based on Ga-polar S-GaN and N-polar M-GaN. Therefore, the UV PDs by integrating the N-polar M-GaN with graphene achieve seven times enhancement in the response compared to that of the Ga-polar S-GaN, demonstrating one of the valuable applications for the GaN polarity modulation from the Ga-polar to N-polar with the assistance of MoS<sub>2</sub> insert layer.

In Figure 6a,d, an opposite photocurrent variation of UV PDs is observed. The current of UV PDs based on the N-polar M-GaN

increases after the UV light irradiation, while it decreases for that of the Ga-polar S-GaN. This trend is further verified by the light-assist KPFM since it can derivate the variations of work function and carrier concentration in the samples (Figure 6b,e). The surface potential measurement of UV PDs is carried out on the top graphene film, which comprises three stages, including the dark condition, irradiated by the UV light, and removal of UV light. Here, the KPFM scans along the Y direction, and the surface potential variation curve is extracted from the KPFM mapping, following the sequence of dark, UV light and removal of light (insets of Figure 6b,e). The measured contact potential ( $V_{CPD}$ ) is the difference between the surface potential of graphene ( $V_{graphene}$ ) and scan tip ( $V_{tip}$ ), which can be written as:

$$V_{CPD} = V_{graphene} - V_{tip} \quad (5)$$

Moreover, the  $V_{CPD}$  can be further defined by the work functions of the tip ( $\phi_{tip}$ ) and the graphene ( $\phi_{graphene}$ ), as given by the equation below:

$$V_{CPD} = \frac{\phi_{tip} - \phi_{graphene}}{e} \quad (6)$$

According to the relationship among the measured contact potential and work function of graphene, there is a negative correlation between these two parameters. For the graphene in the UV PDs based on the Ga-polar S-GaN, its surface potential increases after the UV light irradiation and immediately decreases after the UV light removal. The raised surface potential of graphene corresponds to the reduction of work function, which is calculated to be 0.27 eV based on Equation (6). However, the reduction of surface potential is observed for graphene in the UV PDs based on the N-polar M-GaN at the stage of the UV light irradiation, and it has steadily decreased even after removing the UV light. The adverse surface potential variation of graphene relates to the greatly increased work function, and the calculated value is 0.5 eV, which is larger than the graphene integrated with the Ga-polar S-GaN.

The work function variation of the graphene in the UV PDs is attributed to the fact that the photo-generated carrier in the



GaN absorber drifted into graphene by the interfacial built-in electric field. Here, the energy level schematic diagram of graphene and GaN absorber is proposed to illustrate the carrier transport and work mechanism of these two types of UV PDs, as shown in Figure 6c,f. In the previous work, we prove that the transferred CVD-grown graphene is in the p-type doping as the residual polymer and absorbed oxygen or water in ambient air, resulting in holes as the majority carriers for conduction.<sup>[52]</sup> Therefore, the Fermi level of the graphene carrier transport channel is located below the Dirac point. According to the work function difference between the graphene and GaN absorber, the electron in higher energy level would transit to the lower and make the Fermi level of these two materials at the same position (as marked by the black dash line in Figure 6c,f). At the same time, a space charge region is formed at the interface of graphene and GaN absorber due to the transit of electron, resulting in a built-in electric field. The surface potential of the Ga-polar S-GaN is different from that of the N-polar M-GaN (Figure 3b,e), which makes the built-in electric field in adverse direction as well as the intensity difference.

For the UV PDs based on the Ga-polar S-GaN, there is a built-in electric field pointed from the graphene to GaN, which makes the photo-generated electrons in the GaN absorber drift into the graphene channel (Figure 6c). The followed recombination among the drifted electron and pristine hole in the graphene reduces the measured current, and it agrees with the fact of negative photocurrent of the UV PDs in Figure 6a and the increased graphene surface potential after the UV light irradiation in Figure 6b. The red dash line exhibits the relative position of Fermi level for the graphene after UV light irradiation, and it upshifts toward the Dirac point due to the reduction of majority holes. From the comparison, the MoS<sub>2</sub> insert layer-induced polarity inversion in the N-polar M-GaN has modified its polarized field direction, resulting in an adverse built-in electric field direction pointed from the N-polar M-GaN to graphene. Therefore, the photo-generated holes would drift from the GaN absorber into graphene, and the measured current of the graphene in the UV PDs based on the N-polar M-GaN increases due to the accumulation of majority holes (Figure 6f). At the same time, the corresponding graphene surface potential would decrease (Figure 6e). It indicates that the wider space charge region and stronger built-in electric field are formed because of the large surface work function difference between the separated graphene and N-polar M-GaN. In this way, a mass of photo-generated holes can drift into the graphene through the built-in electric field, which induces the enhanced photocurrent and more significant variation in the surface potential of graphene. In this way, the Fermi level of graphene would downshift away from the Dirac point as the increased concentration of majority holes, and the shifted distance is larger compared to the graphene in the UV PDs based on the Ga-polar S-GaN (as marked by the red dash line in Figure 6f). In Figure 6e, the surface potential for graphene on N-polar M-GaN still goes down after the removal of UV light. It might be attributed to the stronger built-in electric field intensity and lower carrier mobility (Table 2) of N-polar M-GaN, and thus the residual photo-generated carriers would persistently drift into graphene even after the removal of UV light. As marked by the black dashed line in Figure 6e, this

surface potential reduction is weaker than the UV light irradiation condition. The high-response UV PDs by the integration of N-polar M-GaN and graphene demonstrate the feasibility for designing high-performance devices with the polarity modulation of III-nitrides, which can be extended into the other devices, including light-emitting diodes, field-effect transistors, and sensors.

### 3. Conclusion

In conclusion, the direct van der Waals epitaxy and polarity modulation for GaN epilayer by inserting a 2D MoS<sub>2</sub> layer in MOCVD system is reported. Without any growth procedure optimization, the N-polar M-GaN exhibits excellent crystalline quality compared to that of Ga-polar S-GaN in the same batch. Even better, the residual stress in the N-polar M-GaN is nearly eliminated according to the Raman and PL results, indicating that the lattice and thermal mismatch of the epilayer and sapphire substrates are alleviated by the weak van der Waals interaction of MoS<sub>2</sub> insert layers. The surface potential variation and etching effect in the NaOH solution identify the polarity inversion of N-polar M-GaN on the MoS<sub>2</sub> insert layer. The first-principles calculations prove the stronger interaction of Al atoms with the S atoms of MoS<sub>2</sub> and the lower  $E_b$  of N-AlN configuration, which means that the AlN nucleation layer with N-polar is preferred on the MoS<sub>2</sub> insert layer. The UV PDs by integrating the N-polar M-GaN with graphene exhibit a high response of 86.3 A W<sup>-1</sup>, possessing the seven times enhancement compared to that of Ga-polar S-GaN. The light-assist KPFM and energy level distribution prove that the modified polarized field direction of N-polar M-GaN decides the transport behavior of photo-generated carriers, and the similar design can be achieved in other devices.

### 4. Experimental Section

**Growth of Materials:** The c-plane sapphire substrate was ultrasonic cleaned by acetone, ethanol, and deionized water in sequence, and each period persisted to be 5 min. After the sapphire substrate drying by nitrogen gas gun, 2 nm MoO<sub>3</sub> was thermally evaporated on its surface with the basal pressure lower than  $5 \times 10^{-4}$  Pa. The 2 nm MoO<sub>3</sub> film was further annealed in atmosphere at 200 °C for 10 min, which could enhance the compactness of the MoO<sub>3</sub> film. The sulfuration of MoO<sub>3</sub> film was carried out in the dual-temperature zone low-pressure chemical vapor deposition (LPCVD) system, in which S power was placed at the upstream of the input gas (H<sub>2</sub> and Ar) with a relatively low temperature of 140 °C and MoO<sub>3</sub> film on sapphire substrate was placed at the downstream with a higher temperature of 800 °C. The S vapor was transported from the low-temperature zone to the high-temperature zone by the input gas, and the reaction time of MoO<sub>3</sub> and S atoms was counted to be 10 min.

The III-nitrides were grown in the high-temperature MOCVD system, and trimethyl aluminum (TMAI), trimethyl gallium (TMGa), and ammonia (NH<sub>3</sub>) were selected as the source of Al, Ga, and N atoms, respectively. Primarily, the low-temperature AlN nucleation layer was grown at 940 °C for 6 min with the 90 sccm TMAI and 400 sccm NH<sub>3</sub> input gas. Then, the GaN epilayer was grown at a relatively higher temperature of 1080 °C for 66 min, and the flux of TMGa and NH<sub>3</sub> were 144 and 15 000 sccm. The epitaxy process was carried out on both of the sapphire substrates with and without the MoS<sub>2</sub> insert layer.

The monolayer graphene was grown on catalytic Cu foils at the temperature of 1000 °C by the LPCVD system, and CH<sub>4</sub>, H<sub>2</sub>, and Ar were supplied as the carbon source, reduction, and carrier gas, respectively. The reaction chamber was heated up to 1000 °C with the heating rate of 10 °C min<sup>-1</sup>, and 10 sccm H<sub>2</sub> and 100 sccm Ar were supplied during the heating process. The Cu foils was annealed at 1000 °C for 30 min with the persistent H<sub>2</sub> and Ar inputs, which could remove the oxides on copper foils and enlarge its crystal domains. Later, 1 and 3 sccm CH<sub>4</sub> was introduced for 10 and 30 min, achieving the nucleation and coalescence of monolayer graphene film. At the end, the Cu foil/graphene was rapidly cooled down to room temperature by removing the heating cabinet and exposing the reaction chamber in surrounding environment.

**Theoretical Calculations:** First-principles calculations based on density-functional theory (DFT) were performed by employing the generalized gradient approximation (Perdew–Burke–Ernzerhof parametrization, PBE) and projector-augmented wave method, as implemented in the Vienna ab-initio simulation Package (VASP).<sup>[53]</sup> A dispersion correction (DFT-D3) was used to incorporate the long-range van der Waals interaction.<sup>[54,55]</sup> The plane-wave basis set with the kinetic-energy of 500 eV was used. The authors employed 9 × 9 × 1 Monkhorst-Pack k-grids in self-consistent calculations. In addition, the force and total energy convergence thresholds were set to 0.01 eV Å<sup>-1</sup> and 10<sup>-6</sup> eV, respectively. The  $E_b$  is defined as  $E_b = E_{\text{tot}} - E_{\text{slab}} - E_{\text{MoS}_2}$ , and the charge difference ( $\rho_{\text{diff}}$ ) is defined as  $\rho_{\text{diff}} = \rho_{\text{tot}} - \rho_{\text{slab}} - \rho_{\text{MoS}_2}$ , respectively.

**Fabrication of UV PDs:** The monolayer graphene grown on Cu foils was transferred onto the top of GaN epilayers by the universal polymer-assist wetting transfer method. First, the photoresist polymer of S1805G was spin-coated on Cu foil/graphene as the supporting layer. Then, the Cu foil was etched away by Na<sub>2</sub>(SO<sub>4</sub>)<sub>2</sub> solution, and the remaining graphene/S1805G was captured onto the GaN epilayer. At last, the S1805G supporting layer was dissolved into the hot acetone and the monolayer graphene remained on GaN epilayer. Here, the monolayer graphene was simultaneously transferred onto the surface of Ga-polar S–GaN and N-polar M–GaN, which served as the transport channel of the photo-generated carriers in UV PDs due to its high carrier mobility.

A pair of Au electrodes with the thickness of 30 nm was deposited on the surface of monolayer graphene by the thermal evaporation, severing as the carrier collection pads of the UV PDs. The width and spacing of the Au electrode were both 300 μm, which formed a photo-sensitive area of 0.09 mm<sup>2</sup>. For the current measurement, the thick In metal was extruded onto the Au pads.

**Characterization and Measurement:** The Ga-polar S–GaN and N-polar M–GaN were disposed with 85 °C NaOH aqueous solution for various times, then, the surface morphology of GaN was evaluated by the optical microscope (OM; DS-Ri2, Nikon, Japan), atomic force microscope (AFM; MULTIMODE 8, Bruker, US), and scanning electron microscope (SEM; S4800, Hitachi, Japan). The Raman spectra of MoS<sub>2</sub>, GaN, and graphene were measured by the Raman spectrophotometer (LabRAM HR Evolution, HORIBA Scientific, UK) with a 532 nm laser. The X-ray diffraction (XRD; D8 Discover, Bruker, US) was used to identify the crystal quality of GaN. The PL and time-resolved (TR)PL spectra of GaN were excited by a 266 nm laser (MPL-F-266, C. F. Tech., China) and collected with a spectrograph (Omni-λ 300i, Zolix, China). The Hall measurement of GaN was carried out with the off-the-peg equipment (8400 Series, TOYO, Japan), and four In metal columns were extruded onto the corner of the squared GaN epilayer with a perimeter of 32 mm. The surface potential of GaN was measured by Kelvin probe force microscope (KPFM; MULTIMODE 8, Bruker, US), and 15 nm patterned Au lines were deposited on it as the baseline. For the light-assist KPFM, a UV light-emitting diode with 325 nm emission was applied as the light source. The transmission electron microscopy (TEM; Tecnai G2 F20 S-TWIN, FEI, US) integrated with the energy dispersive spectroscopy (EDS) had been used to measure the cross-sectional morphology and element distribution of the N-polar M–GaN.

The current of the UV PDs by integrating the GaN and monolayer graphene was collected by a 2400 Source Meter, KEITHLEY. For each kind of devices, their currents were first measured at dark condition and later illuminated with a 266 nm laser (MPL-F-266-20mW, CNI Laser,

China), in which the scan voltage was varied from 0 to 5 V. The power intensity of the 266 nm laser was regulated to 3 mW and calibrated by a Wattmeter (TP100, CNI Laser, China), corresponding to a power density of 3.8 mW mm<sup>-2</sup>.

## Supporting Information

Supporting Information is available from the Wiley Online Library or from the author.

## Acknowledgements

This work was supported by the National Natural Science Foundation of China (61922078, 62121005, 61827813, 61874118, 52002368), Youth Innovation Promotion Association of the Chinese Academy of Sciences (Y201945, 2019222), Key Research Program of Frontier Sciences, Chinese Academy of Sciences (ZDBS-LY-JSC026), Key Research Program of the Chinese Academy of Sciences (XDPA222), the Open Project of State Key Laboratory of Luminescence and Applications (ET0932A2M1), and the Key-Area Research and Development Program of Guangdong Province (2020B010169001) and Suzhou Institute of Nano-Tech and Nano-Bionics (20Y210).

## Conflict of Interest

The authors declare no conflict of interest.

## Data Availability Statement

Research data are not shared.

## Keywords

MoS<sub>2</sub>, N-polar GaN, polarization electric field, ultraviolet photodetector, van der Waals epitaxy

Received: July 27, 2021

Revised: September 8, 2021

Published online: October 20, 2021

- [1] R. Ramachandran, M. Nymand, *IEEE Trans. Ind. Electron.* **2017**, *64*, 9104.
- [2] A. L. Hickman, R. Chaudhuri, S. J. Bader, K. Nomoto, L. Li, J. C. M. Hwang, H. G. Xing, D. Jena, *Semicond. Sci. Technol.* **2021**, *36*, 044001.
- [3] Y. Ohno, M. Kuzuhara, *IEEE Trans. Electron Devices* **2001**, *48*, 517.
- [4] T. A. Growden, W. Zhang, E. R. Brown, D. F. Storm, D. J. Meyer, P. R. Berger, *Light: Sci. Appl.* **2018**, *7*, 17150.
- [5] H. Amano, R. Collazo, C. D. Santi, S. Einfeldt, M. Funato, J. Glaab, S. Hagedorn, A. Hirano, H. Hirayama, R. Ishii, Y. Kashima, Y. Kawakami, R. Kirste, M. Kneiss, F. M. R. Martin, M. Meneghini, A. Ougazzaden, P. J. Parbrook, S. Rajan, P. Reddy, F. Römer, J. Rusche, B. Sarkar, F. Scholz, L. J. Schowalter, P. Shields, Z. Sitar, L. Sulmoni, T. Wang, T. Wernicke, *J. Phys. D: Appl. Phys.* **2020**, *53*, 503001.
- [6] D. Li, K. Jiang, X. Sun, C. Guo, *Adv. Opt. Photonics* **2018**, *10*, 43.
- [7] K. Jiang, X. Sun, Z. Zhang, J. Ben, J. Che, Z. Shi, Y. Jia, Y. Chen, S. Zhang, W. Lü, D. Li, *Photonics Res.* **2020**, *8*, 1243.

- [8] J. Ben, X. Sun, Y. Jia, K. Jiang, Z. Shi, Y. Wu, C. Kai, Y. Wang, X. Luo, Z. C. Feng, D. Li, *Nanoscale Res. Lett.* **2019**, *14*, 184.
- [9] B. S. Zhang, M. Wu, J. P. Liu, J. Chen, J. J. Zhu, X. M. Shen, G. Feng, D. G. Zhao, Y. T. Wang, H. Yang, A. R. Boyd, *J. Cryst. Growth* **2004**, *270*, 316.
- [10] J. P. Zhang, H. M. Wang, M. E. Gaevski, C. Q. Chen, Q. Fareed, J. W. Yang, G. Simin, M. Asif Khan, *Appl. Phys. Lett.* **2002**, *80*, 3542.
- [11] P. Saengkaew, A. Dadgar, J. Blaessing, T. Hempel, P. Veit, J. Christen, A. Krost, *J. Cryst. Growth* **2009**, *311*, 3742.
- [12] S. J. Bak, D.-H. Mun, K. C. Jung, J. H. Park, H. J. Bae, I. W. Lee, J.-S. Ha, T. Jeong, T. S. Oh, *Electron. Mater. Lett.* **2013**, *9*, 367.
- [13] Z. Chen, X. Zhang, Z. Dou, T. Wei, Z. Liu, Y. Qi, H. Ci, Y. Wang, Y. Li, H. Chang, J. Yan, S. Yang, Y. Zhang, J. Wang, P. Gao, J. Li, Z. Liu, *Adv. Mater.* **2018**, *30*, 1801608.
- [14] J. Yu, L. Wang, Z. Hao, Y. Luo, C. Sun, J. Wang, Y. Han, B. Xiong, H. Li, *Adv. Mater.* **2020**, *32*, 1903407.
- [15] F. Liu, Y. Yu, Y. Zhang, K. C. Jung, T. Wang, X. Zheng, B. Sheng, L. Yang, J. Wei, X. Wang, X. Li, X. Yang, F. Xu, Z. Qin, Z. Zhang, B. Shen, X. Wang, *Adv. Sci.* **2020**, *7*, 2000917.
- [16] S. J. Chae, Y. H. Kim, T. H. Seo, D. L. Duong, S. M. Lee, M. H. Park, E. S. Kim, J. J. Bae, S. Y. Lee, H. Jeong, E.-K. Suh, C. W. Yang, M. S. Jeong, Y. H. Lee, *RSC Adv.* **2015**, *5*, 1343.
- [17] Y. Chen, H. Zang, K. Jiang, J. Ben, S. Zhang, Z. Shi, Y. Jia, W. Lü, X. Sun, D. Li, *Appl. Phys. Lett.* **2020**, *117*, 051601.
- [18] W. Guo, H. Xu, L. Chen, H. Yu, J. Jiang, M. Sheikhi, L. Li, Y. Dai, M. Cui, H. Sun, J. Ye, *J. Phys. D: Appl. Phys.* **2020**, *53*, 483002.
- [19] M. Sheikhi, J. Li, F. Meng, H. Li, S. Guo, L. Liang, H. Cao, P. Gao, J. Ye, W. Guo, *IEEE Trans. Electron Devices* **2017**, *64*, 4424.
- [20] D. Alden, W. Guo, R. Kirste, F. Kaess, I. Bryan, T. Troha, A. Bagal, P. Reddy, L. H. Hernandez-Balderama, A. Franke, S. Mita, C. H. Chang, A. Hoffmann, M. Zgonik, R. Collazo, Z. Sitar, *Appl. Phys. Lett.* **2016**, *108*, 261106.
- [21] D. Alden, T. Troha, R. Kirste, S. Mita, Q. Guo, A. Hoffmann, M. Zgonik, R. Collazo, Z. Sitar, *Appl. Phys. Lett.* **2019**, *114*, 103504.
- [22] W. Guo, H. Sun, B. Torre, J. Li, M. Sheikhi, J. Jiang, H. Li, S. Guo, K.-H. Li, R. Lin, A. Giugni, E. D. Fabrizio, X. Li, J. Ye, *Adv. Funct. Mater.* **2018**, *28*, 1802395.
- [23] Y. Zhang, G. Deng, Y. Yu, Y. Wang, D. Zhao, Z. Shi, B. Zhang, X. Li, *ACS Photonics* **2020**, *7*, 1723.
- [24] Y.-L. Wang, F. Ren, U. Zhang, Q. Sun, C. D. Yerino, T. S. Ko, Y. S. Cho, I. H. Lee, J. Han, S. J. Pearton, *Appl. Phys. Lett.* **2009**, *94*, 212108.
- [25] Y.-L. Wang, B. H. Chu, C. Y. Chang, K. H. Chen, Y. Zhang, Q. Sun, J. Han, S. J. Pearton, F. Ren, *Sens. Actuators, B* **2009**, *142*, 175.
- [26] R. Collazo, S. Mita, A. Aleksov, R. Schlessler, Z. Sitar, *J. Cryst. Growth* **2006**, *287*, 586.
- [27] Q. Sun, Y. S. Cho, B. H. Kong, H. K. Cho, T. S. Ko, C. D. Yerino, I.-H. Lee, J. Han, *J. Cryst. Growth* **2009**, *311*, 2948.
- [28] T. Tanikawa, S. Kuboya, T. Matsuoka, *Phys. Status Solidi B* **2017**, *254*, 1600751.
- [29] S. Keller, N. A. Fichtenbaum, F. Wu, D. Brown, A. Rosales, S. P. DenBaars, J. S. Speck, U. K. Mishra, *J. Appl. Phys.* **2017**, *102*, 083546.
- [30] D. Won, J. M. Redwing, *J. Cryst. Growth* **2013**, *377*, 51.
- [31] G. Martínez-Criado, A. Cros, A. Cantarero, N. V. Joshi, O. Ambacher, M. Stutzmann, *Solid-State Electron.* **2003**, *47*, 565.
- [32] P. R. Tavernier, T. Margalith, J. Williams, D. S. Green, S. Keller, S. P. DenBaars, U. K. Mishra, S. Nakamura, D. R. Clarke, *J. Cryst. Growth* **2004**, *264*, 150.
- [33] F. Liu, Z. Zhang, X. Rong, Y. Yu, T. Wang, B. Sheng, J. Wei, S. Zhou, X. Yang, F. Xu, Z. Qin, Y. Zhang, K. Liu, B. Shen, X. Wang, *Adv. Funct. Mater.* **2020**, *30*, 2001283.
- [34] M. R. Laskar, L. Ma, S. Kannappan, P. S. Park, S. Krishnamoorthy, D. N. Nath, W. Lu, Y. Wu, S. Rajan, *Appl. Phys. Lett.* **2013**, *102*, 252108.
- [35] R. Shahzad, T. W. Kima, S.-W. Kang, *Thin Solid Films* **2017**, *641*, 79.
- [36] G. Plechinger, S. Heydrich, J. Eroms, D. Weiss, C. Schüller, T. Kornm, *Appl. Phys. Lett.* **2012**, *101*, 101906.
- [37] H. Heinke, V. Kirchner, S. Einfeldt, D. Hommel, *Appl. Phys. Lett.* **2000**, *77*, 2145.
- [38] I. Booker, L. R. Khoshroo, J. F. Witok, V. Kaganer, C. Mauder, H. Behnenburg, J. Gruis, M. Heuken, H. Kalisch, R. H. Jansen, *Phys. Status Solidi C* **2010**, *7*, 1787.
- [39] R. Chierchia, T. Böttcher, H. Heinke, S. Einfeldt, S. Figge, D. Hommel, *J. Appl. Phys.* **2003**, *93*, 8918.
- [40] M. Kumar, M. Becker, T. Wernicke, R. Singh, *Appl. Phys. Lett.* **2014**, *105*, 142106.
- [41] L. Bergman, D. Alexson, P. L. Murphy, R. J. Nemanich, M. Dutta, M. A. Strosio, C. Balkas, H. Shin, R. F. Davis, *Phys. Rev. B* **1999**, *59*, 12977.
- [42] J. H. Ryu, Y. S. Katharria, H. Y. Kim, H. K. Kim, K. B. Ko, N. Han, J. H. Kang, Y. J. Park, E.-K. Suh, C.-H. Hong, *Appl. Phys. Lett.* **2012**, *100*, 181904.
- [43] J. Wei, R. Neumann, X. Wang, S. Li, S. Fündling, S. Merzsch, M. A. M. Al-Suleiman, Ü. Sökmen, H.-H. Wehmann, A. Waag, *Phys. Status Solidi C* **2011**, *8*, 2157.
- [44] W. Guo, L. Chen, H. Xu, Y. Qian, M. Sheikhi, J. Hoo, S. Guo, L. Xu, J. Liu, F. Alqatari, X. Li, K. He, Z. C. Feng, J. Ye, *Photonics Res.* **2020**, *8*, 812.
- [45] J. Jiang, Y. Zhang, F. Yang, Z. Huang, L. Yan, P. Li, C. Chi, D. Zhao, B. Zhang, G. Du, *Vacuum* **2015**, *119*, 63.
- [46] H. P. Maruska, J. J. Tietjen, *Appl. Phys. Lett.* **1959**, *15*, 327.
- [47] T. K. Zywiets, J. Neugebauer, M. Scheffler, *Appl. Phys. Lett.* **1999**, *74*, 1695.
- [48] B. Monemar, P. P. Paskov, J. P. Bergman, G. Pozina, A. A. Toropov, T. V. Shubina, T. Malinauskas, T. Malinauskas, *Phys. Rev. B* **2010**, *82*, 235202.
- [49] G. Callsen, M. R. Wagner, T. Kure, J. S. Reparaz, M. Bügler, J. Brunnmeier, C. Nenstiel, A. Hoffmann, M. Hoffmann, J. Tweedie, Z. Bryan, S. Aygun, R. Kirste, R. Collazo, Z. Sitar, *Phys. Rev. B* **2012**, *86*, 075207.
- [50] X. W. Wang, S. R. Xu, J. J. Du, R. S. Peng, X. M. Fan, Y. Zhao, W. Li, J. C. Zhang, Y. Hao, *Mater. Lett.* **2019**, *253*, 314.
- [51] Z. M. Shi, X. J. Sun, Y. P. Jia, X. K. Liu, S. L. Zhang, Z. B. Qi, D. B. Li, *Sci. China: Phys., Mech. Astron.* **2019**, *62*, 127311.
- [52] Y. Chen, N. Zhang, Y.-F. Li, Y.-G. Bi, Y.-Y. Yue, J. Feng, H.-B. Sun, *Adv. Opt. Mater.* **2018**, *6*, 1701348.
- [53] G. Kresse, D. Joubert, *Phys. Rev. B* **1999**, *59*, 1758.
- [54] S. Grimme, *J. Comput. Chem.* **2006**, *27*, 1787.
- [55] V. Barone, M. Casarin, D. Forrer, M. Pavone, M. Sambri, A. Vittadini, *J. Comput. Chem.* **2009**, *30*, 934.